Research Paper

Impact of chemical modeling on the numerical analysis of a LOx/GCH4 rocket engine pintle injector

L. Lucchese [a,*], J. Liberatori [a], D. Cavalieri [a], D. Simone [b], D. Liuzzi [b], M. Valorani [a], P.P. Ciottoli [a]

[a] *Department of Mechanical and Aerospace Engineering, Sapienza University of Rome, Via Eudossiana, 18, Rome, 00184, Italy*
[b] *Avio S.p.A, Via Ariana, km 5.2, Colleferro, 00034, Italy*

ARTICLE INFO

ABSTRACT

Liquid rocket engines equipped with LOx/GCH4 pintle injectors represent a promising technology when a large throttling capability is required. Still, limited amounts of data are available in the literature about the numerical characterization of pintle injector configurations under reacting conditions, with the entirety of these studies resorting to global or quasi-global reaction mechanisms. To this end, the objective of the present work is to assess the impact of chemical kinetic modeling on the prediction of major combustion observables, thermal flow field, and gas–liquid interaction in a pintle configuration of interest. Specifically, we carry out three unsteady Reynolds-averaged Navier–Stokes simulations under an Eulerian–Lagrangian fashion through variable-fidelity kinetic schemes, namely, one quasi-global scheme and two skeletal schemes derived from the high-pressure Zhukov's detailed mechanism. On the one hand, employing quasi-global chemical kinetics delivers an inconsistent flame topology. On the other hand, the overall combustion characteristics remain unaltered regardless of the skeletal mechanism complexity, while significant discrepancies can be envisaged in the flame dynamics. Moreover, the computational burden exponentially increases with mechanism size, preventing high-fidelity skeletal schemes from being leveraged in design-oriented computational fluid dynamics. Based on these findings, quasi-global chemical kinetics should be discarded when targeting high-pressure rocket engine conditions, while ad-hoc optimized skeletal mechanisms should be developed. This way, the present study provides an insightful contribution to identifying the optimal complexity of chemical kinetic modeling to ensure reliable, still cost-effective numerical simulations of liquid rocket engine combustion devices.

1. Introduction

Liquid rocket engines (LREs) represent the most widely used technology to fulfill the increasing interest in access to space and its exploration. From the earliest LRE-featured missions, the selection of suitable propellant combinations has been the subject of a continuously evolving development process, targeting a trade-off between engine performance, bulkhead architecture, system reliability, and safe handling of the propellants. In recent years, methane–oxygen has emerged as a breakthrough combination to revolutionize the space economy. Notably, methane exhibits remarkable advantages compared with heavier hydrocarbon and hydrogen options. On the one hand, the combined effect of delivering higher specific impulse and less likely coking phenomena and soot formation [1] makes methane a promising alternative to denser non-cryogenic hydrocarbons, such as RP-1. On the other hand, although providing less attractive engine performance levels than hydrogen, high density and boiling point close to that of oxygen

promote the adoption of cheaper and lighter storage and feed systems in methane-fueled rocket engines [2]. Additionally, the methane–oxygen combination is the current favorite choice when investigating the possibility of in-situ resource utilization (ISRU) in the context of interplanetary space exploration [3]. Besides the selection of suitable propellant combinations, thrust modulation is pivotal for effective, autonomous, and sustainable access to space, being crucial in most of the mission profiles: (i) trajectory control, (ii) planetary entry and descent, (iii) and the ability to continuously follow the most economical thrust curve in a given situation instead of making discrete throttling changes over a few select operating points. The pintle injector is a natural choice when a large throttling range is required [4], given that ad-hoc propellant control systems and strategies aimed at restraining thermal loads on the injector element are necessary. A series of successful applications throughout the history of LREs demonstrated the deep throttling capabilities of the pintle technology. Specifically, these

---

include the Apollo low-thrust lunar descent engine (thrust ratio 10:1), fueled with monomethylhydrazine (MMH) and nitrogen oxides [5], the main engine of the Chang'e-3 lunar probe mission (thrust ratio 5:1) [6], and the Merlin 1D engine of the Falcon 9 rocket.

In recent years, extensive efforts have been devoted to investigating pintle mixing and combustion characteristics both experimentally and numerically. From an experimental standpoint, most research studies focused on spray characterization. The experimental measurements delivered ad-hoc empirical correlations and theoretical spray models to correlate the major spray observables, e.g., the Sauter mean diameter (SMD), with geometrical features and non-dimensional parameters [7]. Specifically, the main outcomes of these researches highlighted that the spray pattern and mixing efficiency in both liquid–liquid and liquid–gas pintle injectors was mostly impacted by: (i) the total momentum ratio (TMR), i.e., the ratio of propellant momentum fluxes [8–10]; (ii) the width of the pintle slots [11]; (iii) the gas and liquid Reynolds [12] and Weber numbers [13]; (iv) the annular orifice area of the fuel passage [14]; (v) the skip distance, defined as the distance between the annulus end section and the fuel-oxidizer impingement location [15]. Conversely, a limited amount of experimental data is available from the open literature regarding hot firing tests, predominantly focusing on the combustion efficiency of pintle configurations and overheating issues on the tip of the injector element. In this regard, Vasques and Haidn [16] investigated four liquid oxygen (LOx) - liquid methane (LCH4) pintle injector configurations, differing in the value of the skip distance and the presence of an active cooling strategy acting on the pintle tip and a deflecting ramp for the fuel annular flow. The tests outlined the importance of the deflector to substantially enhance the pintle tip life, although a decrease in combustion efficiency was observed. At the same time, actively cooling the injector element had a negligible impact on the engine performance. In [17], Son et al. carried out a series of experimental measurements on gaseous oxygen (GOx) - gaseous methane (GCH4) pintle injector, focusing on how the width of the pintle injector slots affects the flame pattern through CH* chemiluminescence and Schlieren imaging techniques. In particular, their analysis revealed that different values of pintle opening distance, namely, different values of oxygen injection momentum fluxes, resulted in two peculiar anchoring mechanisms, i.e., the shear layer flame and the tip-attached flame. Lastly, Kang et al. [18] investigated a LOx-kerosene pintle injector in hot firing tests under supercritical conditions. The authors highlighted overheating issues on the pintle tip due to the peculiar flow field within the combustion chamber, resulting in hot combustion products recirculating in the proximity of the chamber axis. To mitigate thermal damage, an insert nozzle was designed to enhance pintle tip cooling.

On the other hand, the majority of numerical studies were devoted to the assessment of empirical and theoretical spray models developed starting from experimental campaigns under cold-flow conditions [8, 13,15,19]. As already outlined concerning experimental measurements, a restricted amount of numerical investigations focused on characterizing combustion characteristics and performance of pintle injector engines. In [20], Son et al. performed steady axisymmetric simulations on a GOx-GCH4 pintle injector configuration, adopting the 6-step Jones-Lindstedt mechanism developed by Frassoldati et al. for methane–oxygen combustion [21] and modeling turbulent combustion through the eddy dissipation concept (EDC) model [22]. The authors provided detailed insights into combustion efficiency trends at varying mass flow rate conditions, i.e., under different thrust levels, envisaging a possible solution to maintain acceptable performances by modifying the pintle opening distance. In [23], Fang and Shen modeled a LOx/GCH4 pintle injector by resorting to an Eulerian–Lagrangian hybrid approach while characterizing chemical processes and turbulent combustion via a single-step reaction mechanism and EDC, respectively. The authors investigated the effects on the combustion efficiency given by the skip distance, the width of the pintle

orifices, and the characteristic length of the combustor. In particular, an optimal value for the skip distance was observed around 1.0 regarding the optimization of the combustion efficiency, while the latter reportedly decreased with increasing pintle opening distance. In previous work by our research group [24], Liberatori et al. investigated two LOx/GCH4 pintle injector configurations, characterized by a skip distance of 1.0 and 1.5, respectively, via three-dimensional unsteady Reynolds-averaged Navier–Stokes (uRANS) simulations under an Eulerian–Lagrangian fashion. In particular, the authors adopted an uncertainty quantification (UQ) framework to assess the impact of LOx droplet size distribution at the injection section on major observables. The outcome of this analysis demonstrated that the modeling of liquid injection could not overshadow the sensitivity of temperature and velocity fields to the selection of a specific skip distance. Lastly, to provide a quantitative estimation of the insert nozzle on the cooling of the pintle tip, Kang et al. [18] carried out uRANS computations, coupled with a conjugate heat transfer analysis, which returned a reduction up to 21.4% in the pintle tip temperature.

Therefore, although the pintle injector represents a promising technology for thrust modulation in LRE applications, a limited amount of numerical studies on configurations of interest are available. At the same time, an adequate numerical characterization of LRE thrust chambers equipped with pintle injectors is crucial to driving design-oriented computational fluid dynamics (CFD) approaches. Moreover, existing numerical investigations rely on global or quasi-global reaction schemes, which may be unsuitable for capturing peculiar flame patterns observed during the experimental campaigns.

Based on these considerations, in the present work, we provide a set of three-dimensional uRANS simulations on the LOx/GCH4 pintle injector configuration investigated by Fang and Shen [23], and Liberatori et al. [24] through variable-fidelity reaction schemes. One semi-global and two skeletal kinetic mechanisms are employed to assess the impact of chemical kinetic modeling on combustion characterization in this category of devices. Hence, the paper is organized as follows. In Section 2, we describe the theoretical model and numerical setup pursued throughout the work. Section 2.1 provides an overview of the hybrid Eulerian–Lagrangian uRANS framework, along with the full set of governing equations and the adopted closure models. In Section 2.2, we discuss the selection of three variable-fidelity chemical reaction mechanisms. In Section 2.3, we outline the test case configuration under study and the computational domain setup. Section 3 illustrates the outcome of the numerical investigations provided by different reaction schemes, with a detailed description of how chemical kinetic modeling impacts the major combustion observables. Lastly, in Section 4, we summarize the key results.

2. Theoretical model and numerical setup

In this section, we outline the fundamental aspects of the adopted numerical framework, and we provide an overview of the investigated test case.

2.1. Governing equations

The uRANS Eulerian–Lagrangian numerical approach [25–28] is described in this section. On the one hand, the liquid phase is modeled through statistic parcels, whose evolution is treated according to a Lagrangian fashion. On the other hand, the ensemble average of the turbulent Eulerian gas phase equations in three-dimensional conservative form read:

$$\frac{\partial \overline{\rho}}{\partial t} + \frac{\partial (\overline{\rho}\tilde{u}_j)}{\partial x_j} = \overline{S}_m, \tag{1}$$

$$\frac{\partial (\overline{\rho}\tilde{u}_i)}{\partial t} + \frac{\partial}{\partial x_j}\left[\overline{\rho}\tilde{u}_i\tilde{u}_j + \overline{p}\delta_{ij} - \tilde{\tau}_{ij} - \overline{\rho u_i' u_j'}\right] = \overline{\rho}g_i + \overline{S}_{p,i}, \tag{2}$$

$$\frac{\partial \overline{\rho} \tilde{h}_t}{\partial t} + \frac{\partial}{\partial x_j}\left[\overline{\rho} \tilde{h}_t \tilde{u}_j + \tilde{q}_j\right] = \frac{\partial \overline{p}}{\partial t} + \rho(\tilde{u}_i g_i) + \overline{S}_h + \dot{\omega}_h, \tag{3}$$

$$\frac{\partial \overline{\rho} \tilde{y}_i}{\partial t} + \frac{\partial}{\partial x_j}\left[\overline{\rho} \tilde{y}_i \tilde{u}_j + \tilde{J}_j + \overline{\rho} \tilde{u}_j' \tilde{y}_i'\right] = \overline{S}_{m,i} + \dot{\omega}_i. \tag{4}$$

The "overbar" indicates the Reynolds average, while the "tilde" superscript represents the Favre average. Moreover, ρ is the density, u_i is the velocity in direction i, p is the pressure, δ_{ij} is the Kronecker delta symbol, τ is the viscous stress tensor, g_i is the gravity acceleration in direction i, h_t is the total enthalpy, given by the sum of sensible enthalpy and kinetic energy, q is the heat transfer rate modeled assuming a unitary turbulent Prandtl number, y_i is the mass fraction of species i, J is the diffusive mass flux, $\dot{\omega}_h$ and $\dot{\omega}_i$ represent the reaction source terms for the sensible enthalpy and species i, respectively. The term $\overline{\rho u_i' u_j'}$ represents the Reynolds stress tensor, modeled via the $k - \epsilon$ closure, while $\overline{\rho} \tilde{u}_j' \tilde{y}_i'$ is the turbulent mass flux, closed through a gradient-diffusion assumption with unitary turbulent Schmidt number.

The terms representing the coupling between the Eulerian carrier phase and the Lagrangian liquid droplets in terms of mass, momentum, and energy exchange are:

$$S_m = -\sum_{k=1}^{N} \frac{dm_{p,k}}{dt} \delta(x - x_{p,k}), \tag{5}$$

$$S_p = -\sum_{k=1}^{N} \frac{d(m_{p,k} u_{p,k})}{dt} \delta(x - x_{p,k}), \tag{6}$$

$$S_h = -\sum_{k=1}^{N} \frac{d(m_{p,k} c_{p,k} T_{p,k})}{dt} \delta(x - x_{p,k}), \tag{7}$$

where N indicates the overall number of liquid parcels in the computational domain, $m_{p,k}, u_{p,k}, c_{p,k}, T_{p,k}, x_{p,k}$ are the mass, velocity, specific heat capacity, temperature, and position of parcel k, respectively, and δ denotes the Dirac delta function.

At the same time, the governing equations for the kth computational parcel read in a Lagrangian fashion:

$$\frac{dm_{p,k}}{dt} = \dot{m}_{p,k}, \tag{8}$$

$$m_{p,k} \frac{d\boldsymbol{u}_{p,k}}{dt} = \boldsymbol{F}_{p,k}, \tag{9}$$

$$m_{p,k} c_{p,k} \frac{dT_{p,k}}{dt} = \dot{m}_{p,k} l_{v,k} + A_{p,k} h_{p,k}(T - T_{p,k}), \tag{10}$$

$$\frac{d\boldsymbol{x}_{p,k}}{dt} = \boldsymbol{u}_{p,k}, \tag{11}$$

describing the conservation of mass (Eq. (8)), momentum (Eq. (9)), and energy (Eq. (10)), as well as the trajectory of the droplets (Eq. (11)). Specifically, $\dot{m}_{p,k}$ in Eq. (8) denotes the mass vaporization rate, while the aerodynamic force in Eq. (9), consisting of drag only, is modeled through the Schiller–Naumann correlation [29]. In Eq. (10), the parcel temperature evolution is driven by the latent heat of vaporization, $l_{v,k}$ and the convective heat exchange, with $h_{p,k}$ denoting the convective heat coefficient and T indicating the gas phase temperature.

We employ an in-house version of the pressure-based *sprayFoam* solver natively supplied within the OpenFOAM CFD toolbox [30], namely, *rocketSprayFoam*. Additional details about the numerical framework and the implementation of LOx properties into the *rocketSprayFoam* solver can be found in previous works by our research group [24, 31].

The pressure–velocity coupling is realized through the PIMPLE algorithm, while turbulent combustion is modeled through EDC. Liquid phase parcels are injected into the computational domain following a monodisperse distribution to simulate the primary atomization process, with a fixed diameter of 50 µm, whereas secondary atomization is modeled adopting the Reitz-Diwakar breakup model [32]. Lastly, the discretization schemes ensure second-order spatial and first-order time accuracy, with a maximum Courant number set to 0.2 to ensure stability, resulting in a physical time-step of approximately $1 \cdot 10^{-7}$ s.

Table 1
Geometrical features of the pintle injection system and combustion chamber, along with the characteristic sizes of the LOx quadrangular slot.

Geometrical dimensions				Slot size	
D_p [mm]	D_{ann} [mm]	L_s/D_p [–]	D_c/D_p [–]	l [mm]	w [mm]
30	34	1	3.3	2.95	2

2.2. Chemical kinetic modeling

From the open literature, many detailed chemical mechanisms are available to characterize methane oxidation [33–38]. Nonetheless, only a few of these high-fidelity reaction schemes include the high-pressure reaction pathways typical of methane–oxygen combustion under LRE-relevant conditions, an extensive review of the latter being reported in [39]. Furthermore, detailed kinetic mechanisms are not affordable when targeting large-scale CFD simulations of methane–oxygen flames in rocket engines [40,41], as retaining a large number of chemical species results in highly stiff systems of ordinary differential equations (ODEs) due to largely different timescales and prohibitive computational cost [42].

At the same time, adopting global or quasi-global reaction schemes [43,44] and reduced mechanisms derived by applying ad-hoc strategies [45–50] to detailed kinetic schemes may allow cost-efficient, large-scale CFD simulations while reproducing the global features of interest of a given combustion process. Still, an optimal degree of complexity of these simplified mechanisms, trading off accuracy for computational costs [51], should be identified to perform vast and reliable numerical campaigns on LRE combustion devices.

Based on these considerations, the present work illustrates how using variable-fidelity, compact kinetic mechanisms affects the prediction of the major combustion observables, such as the characteristic flame topology, in the LRE pintle injector configuration under examination. Specifically, we conduct the numerical analysis by adopting: (i) the 9-species Jones-Lindstedt mechanism formulated by Frassoldati et al. [21], hereinafter denoted as JL-9, which introduces two additional reaction steps, i.e., the dissociation reactions of water and oxygen, in the standard 6-species Jones-Lindstedt [44] scheme to address methane–oxygen combustion; (ii) a 13-species skeletal mechanism, derived in [39] through a simplification algorithm [52,53] based on computational singular perturbation (CSP) theory [54] - and exploiting the tangential stretching rate (TSR) analysis [55] - from the C_1-C_4 version of the 207-species high-pressure detailed mechanism by Zhukov [38], and hereinafter denoted as TSR-CDF-13; notably, the TSR-CDF-13 scheme was obtained from a training dataset of methane–oxygen one-dimensional counterflow diffusion flames, and targets chemical processes in complex thrust-chamber flow fields inducing moderate flame aerodynamic straining; (iii) a 24-species skeletal mechanism, derived in [39] by applying the CSP-TSR algorithm to Zhukov's detailed scheme [38], and hereinafter denoted as TSR-GP-24; notably, TSR-GP-24 is a general-purpose scheme, obtained from a comprehensive training dataset including thermochemical states from methane–oxygen zero-dimensional constant-pressure batch reactors, one-dimensional counterflow diffusion and premixed flames, and partially stirred reactors (PSRs), and targets complex thrust-chamber flow fields possibly inducing flame extinction.

2.3. Test case description

The computational domain encompasses the pintle injector configuration similar to that already investigated in [23,24]. Specifically, the longitudinal extension of the present domain is 405 mm, while the converging-diverging nozzle is not included. To carry out three-dimensional uRANS simulations while retaining an affordable computational burden, a 22.5° sector of the full pintle configuration is
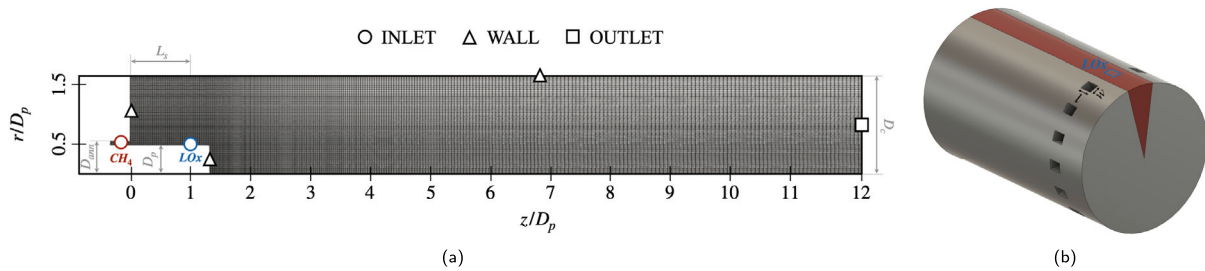
Fig. 1. Schematic representation of the pintle injector configuration under study: (a) computational domain, along with geometrical dimensions and boundary conditions, (b) close-up of the quadrangular LOx slots on the pintle injector element, featured with its characteristic sizes and the 22.5° sector (red) investigated via CFD. (For interpretation of the references to color in this figure legend, the reader is referred to the web version of this article.)
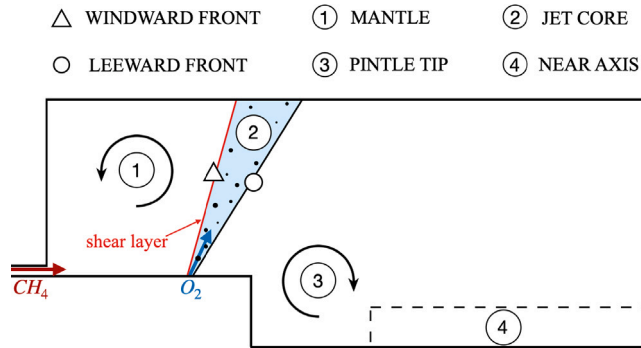

Fig. 2. Schematic representation of the cross-flow typical of the pintle injector, with main areas in the field marked and labeled.

investigated, resulting in the presence of one oxygen quadrangular slot on the pintle injector element. A schematic representation of the computational domain, which is discretized by a fully structured hexahedral mesh of 300k cells, is reported in Fig. 1. In this regard, the adopted mesh resolution follows from a grid convergence study about the uRANS simulations equipped with the TSR-CDF-13 kinetic scheme, which is not reported here for the sake of brevity. The fundamental geometrical dimensions of the pintle injection system and combustion chamber are summarized in Table 1. Notably, from the characteristic sizes of the LOx quadrangular slot, it is possible to derive the value of the blockage factor, $BF = (Nw)/(\pi D_p) = 0.35$, which is known to express the percentage of annular methane inflow impinging on the radial LOx cross-flow. Here, $N = 16$ denotes the total number of liquid oxygen orifices in the fully three-dimensional geometry, while $D_p = 30$ mm is the pintle injector diameter.

The gaseous methane and liquid oxygen injection conditions are illustrated in Table 2. As may be noted, fuel and oxidizer mass flow rates slightly differ from those employed in [23], resulting in an oxidizer-to-fuel ratio $O/F = 3$. Moreover, the total momentum ratio, defined as $TMR = (\dot{m}_f v_f)/(\dot{m}_{ox} v_{ox})$, takes a value of 0.48. Furthermore, the operating pressure is 37.5 bar.

For what concerns the adopted boundary conditions, GCH4 and LOx mass flow rates are imposed at the corresponding inflow sections, all walls are treated as viscous and adiabatic, with standard wall-functions employed for the wall interaction [56], and a Dirichlet condition on pressure, i.e., $p = 37.5$ bar, is defined at the outlet section. A schematic representation of the typical cross-flow structure characterizing pintle injectors is displayed in Fig. 2, the main zones in the flow are marked and labeled to provide a reference for the upcoming discussion. From now on, the mean fields shown will be derived through an averaging operation performed once a statistical steady state condition is reached for each test case. In particular, we determine the statistical steady state as a result of an averaging procedure conducted over two consecutive time windows, spanning over a time period equal to 5 flow-through

Table 2
Operating conditions of the pintle injection system regarding the fuel (f) and oxidizer (ox) sides.

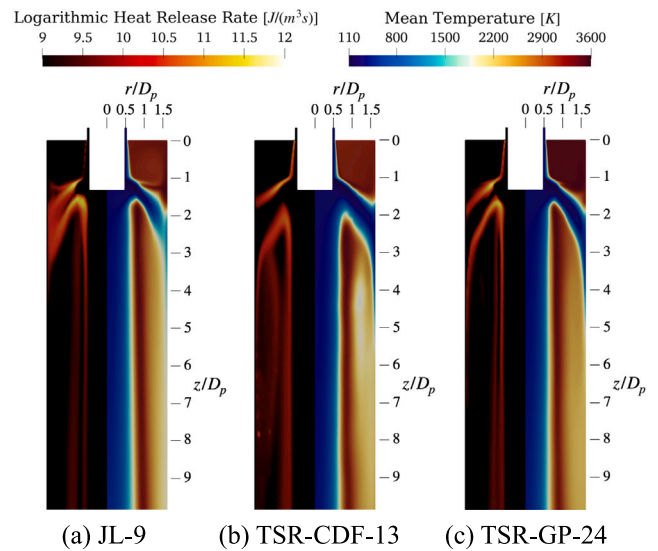| Mass flow rate		Velocity		Temperature		Pressure
$\dot{m}_f$ [kg/s]	$\dot{m}_{ox}$ [kg/s]	v_f [m/s]	v_{ox} [m/s]	T_f [K]	T_{ox} [K]	P_c [bar]
0.71	2.13	136	21.9	293	110	37.5

Fig. 3. Mean logarithmic heat release rate (left) and temperature (right) contour maps over a central slice of the computational domain, as predicted by: (a) JL-9 scheme, (b) TSR-CDF-13 scheme, (c) TSR-GP-24 scheme.

times (FTs), with $FT = L_c/v_{conv}$, where $L_c = 0.405$ m is the longitudinal extension of the computational domain, and $v_{conv} \approx 40$ m/s is the characteristic convection velocity estimated according to [57].

3. Results and discussion

The following discusses the major combustion observables returned by the three kinetic mechanisms. In particular, we present the most significant differences in terms of flame topology, thermal flow field, gas–liquid phase interaction, and combustion efficiency so as to assess the sensitivity to the chemical kinetic modeling.

Firstly, Fig. 3 illustrates the mean temperature and logarithmic heat release rate, i.e., $\log(\overline{\dot{\omega}}_h)$, hereinafter denoted as HRR, predicted by the three chemical mechanisms over a central slice of the computational domain placed along the LOx quadrangular slot, as shown in Fig. 1(b). As noted from the logarithmic heat release rate contour maps, regardless of the kinetic scheme, the pintle injector configuration under study exhibits a shear-layer flame, defined by Son et al. [17] as
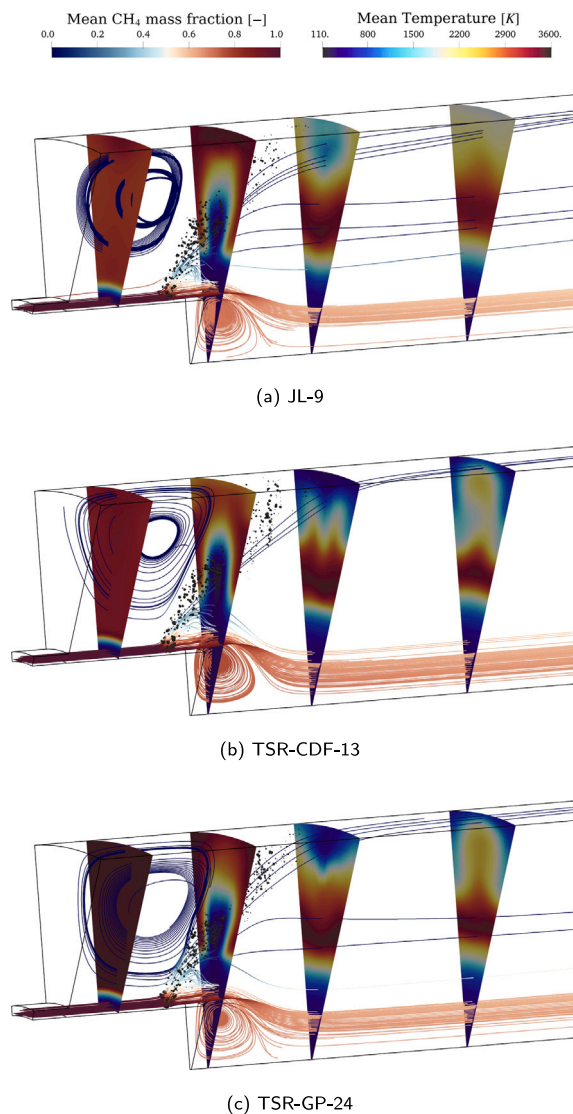
Mean CH₄ mass fraction [–]
0.0 0.2 0.4 0.6 0.8 1.0

Mean Temperature [K]
110. 800 1500 2200 2900 3600.

(a) JL-9

(b) TSR-CDF-13

(c) TSR-GP-24

Fig. 4. Three-dimensional visualization of the thermal flow field in the pintle injector configuration under study: (a) JL-9 scheme, (b) TSR-CDF-13 scheme, (c) TSR-GP-24 scheme. Mean velocity field streamlines are colored by mean CH_4 mass fraction, while LOx parcels are scaled by their diameter. The mean temperature distribution is shown over four slices of the computational domain, located at $z/D_p = 0.5$, 1.5, 2.5, and 4. (For interpretation of the references to color in this figure legend, the reader is referred to the web version of this article.)

a flame characterized by a thin flame-sheet anchored to the injector face. Notably, the tip-attached anchoring mechanism reported in [17], and characterized by a shorter flame sheet attached to the pintle tip, cannot take place due to the low value of BF, which results in a restrained amount of annular methane inflow impinging on the radial LOx cross-flow. As a result, the near-axis region of the combustion chamber shows extremely low temperature, thus avoiding any flame anchoring in the proximity of the pintle post tip. On the contrary, the selection of the chemical mechanism affects the longitudinal extension of the cold oxygen core. Indeed, the quasi-global chemical kinetics characterizing the JL-9 scheme drastically affects the ignition of the mixture once the gaseous methane and the evaporated oxygen come into contact around the LOx radial cross-flow, as further discussed in the remainder of the present section. This aspect is corroborated by the spatial distribution of the heat release rate, which completely surrounds the cold oxygen jet core when employing the JL-9 mechanism. On the other hand, the low-temperature region induced by LOx evaporation is

more prominent in case the skeletal kinetic mechanisms, namely, TSR-CDF-13 and TSR-GP-24, are adopted. Concerning the kinetic schemes derived by reducing Zhukov's high-pressure detailed mechanism, the flame front does not surround the cold oxygen core; in contrast, two distinct peak-level zones of HRR can be envisaged on both sides of the LOx radial cross-flow. Moreover, it is worth highlighting from the beginning that the TSR-CDF-13 vaporization-induced low-temperature region exhibits a larger extension compared with that predicted by TSR-GP-24 as a consequence of local quenching phenomena, which are illustrated in detail in the following. These quenching characteristics lead to a shedding of cold gaseous oxygen pockets, which are reflected in the mean temperature distribution. In fact, a medium-temperature region can be distinguished downstream of the flame front, namely, between $z/D_p = 3$ and $z/D_p = 6$, as a result of the shedding process.

In Fig. 4 is shown a three-dimensional visualization of the mean temperature field predicted by the three chemical kinetic mechanisms, accompanied by mean velocity streamlines colored by methane mass fraction and a representative population of liquid parcels, scaled by their diameter. Specifically, two distinct reverse flow regions can be distinguished: (i) the mantle recirculation zone, induced by the impingement of the methane annular flow onto the liquid oxygen cross-flow, and (ii) the core recirculation zone, caused by a backward-facing-step phenomenon in the proximity of the pintle tip, both zones are also schematically displayed in Fig. 2 and denoted as mantle, and pintle tip. Regardless of the kinetic scheme by which the numerical analysis is carried out, no significant differences can be envisaged in the flow structure and extension of the recirculation regions. Moreover, it is worth highlighting that, due to the adopted value of the blockage factor, BF, a prominent methane bypass is observed around the LOx slot. As a result, the near-axis region of the combustion chamber features a cold and methane-rich zone. Conversely, adopting different kinetic mechanisms results in slight differences in the flame extension – characterized by the logarithmic heat release rate levels – toward the upper solid wall of the chamber, consistently with what is illustrated in Fig. 3. Furthermore, Fig. 4(a) shows that the JL-9 scheme provides a restrained penetration of cold gaseous oxygen in the upper region, compared with the CSP-TSR skeletal mechanisms.

In Fig. 5, a quantitative comparison between the chemical kinetic mechanisms in terms of the mean temperature field is performed, focusing on the radial distributions in correspondence with various axial locations in the computational domain. As anticipated by Fig. 3, and as can be noted from Fig. 5(a), the mean temperature distribution in the mantle recirculation zone predicted by the TSR-GP-24 scheme exhibits higher levels compared with the JL-9 and TSR-CDF-13 outcomes. Furthermore, Fig. 5(c), which refers to the region close to the leeward flame front, i.e., $z/D_p = 2.5$, highlights slight differences in the mean temperature predictions by the three kinetic mechanisms due to the characteristic thickness of the cold oxygen jet. In particular, the skeletal schemes show a faster decay of the mean temperature levels, namely, between $r/D_p = 1$ and $r/D_p = 1.3$, as opposed to the quasi-global mechanism. Fig. 5(d) provides further insights into the oxygen-pocket shedding phenomenon observed when employing the TSR-CDF-13 kinetic scheme, as the latter predicts a decrease up to 25% of the mean temperature downstream of the leeward flame front zone. Lastly, as illustrated in Fig. 5(f), in the proximity of the outflow section, the JL-9 reaction mechanism delivers overall lower temperature values compared with the CSP-TSR skeletal schemes, which directly impacts the predicted combustion efficiency, as further discussed in the following.

Significant discrepancies amongst the chemical mechanisms arise in the mixture fraction space, reflecting different flame structures induced by how the kinetic behavior is modeled. In this regard, Fig. 6 illustrates the distribution of the instantaneous temperature fields as a function of the mixture fraction, Z, computed according to the Bilger's definition [58], along with two one-dimensional flamelets predicted by the Zhukov's detailed mechanism [38], from which the TSR-CDF-13 and
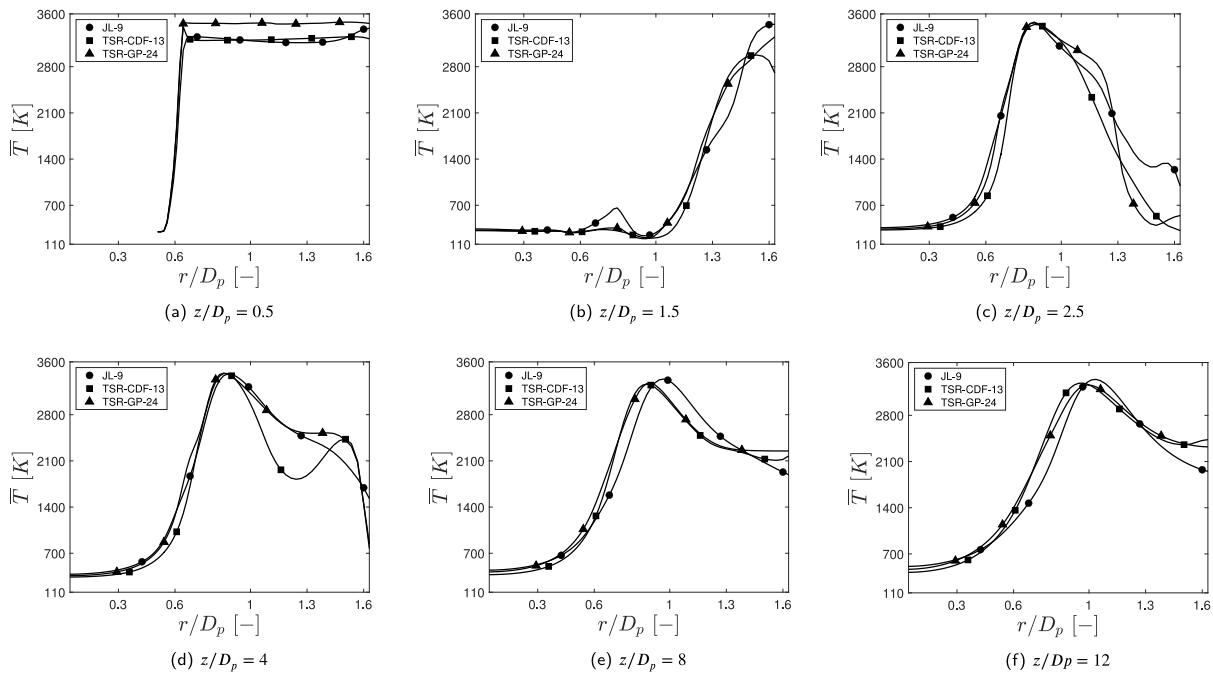
Fig. 5. Radial distribution of the mean temperature predicted by the three chemical kinetic mechanisms: (a) $z/D_p = 0.5$, (b) $z/D_p = 1.5$, (c) $z/D_p = 2.5$, (d) $z/D_p = 4$, (e) $z/D_p = 8$, (f) $z/D_p = 12$.
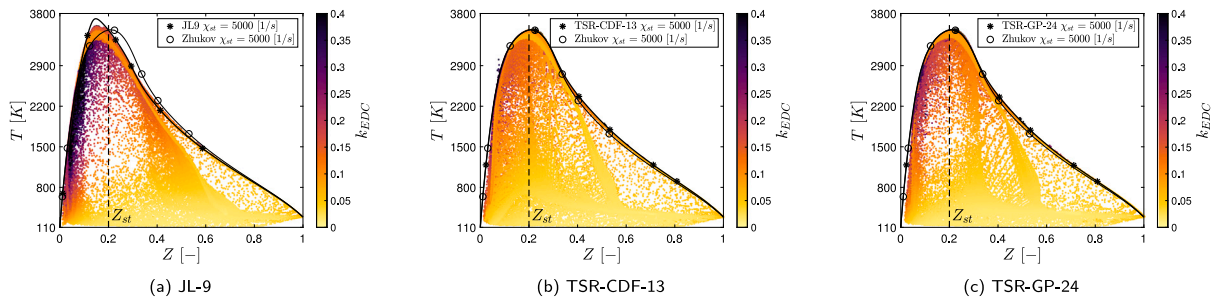

Fig. 6. Instantaneous temperature fields as a function of the mixture fraction, Z, as predicted by: (a) JL-9 scheme, (b) TSR-CDF-13 scheme, (c) TSR-GP-24 scheme. Each point is color-coded with the EDC mixing factor, k_{EDC}. Solid lines represent one-dimensional flamelets predicted by the detailed Zhukov's mechanism, and by the schemes under study, at a value of stoichiometric scalar dissipation $\chi_{st} = 5000 \; 1/s$.
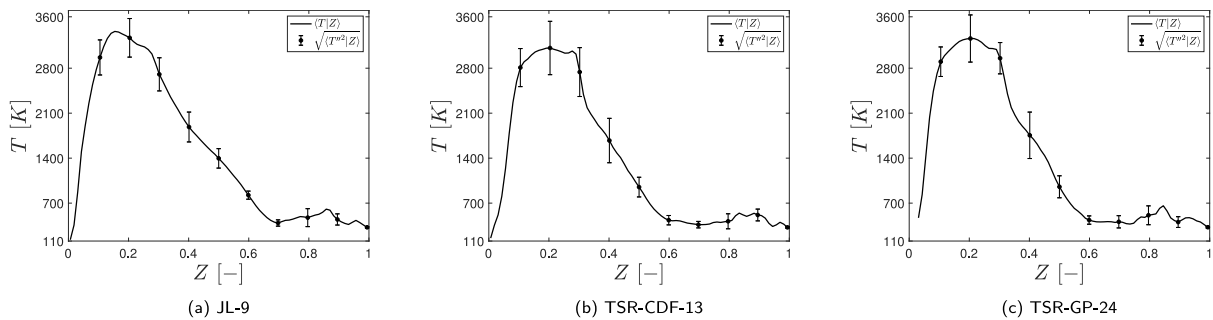

Fig. 7. Conditional mean (solid lines) and rms (error bars) of temperature as a function of the mixture fraction, Z, as predicted by: (a) JL-9 scheme, (b) TSR-CDF-13 scheme, (c) TSR-GP-24 scheme.

TSR-GP-24 mechanisms were obtained [39], and by the mechanisms under study. Precisely, the latter are calculated at a stoichiometric scalar dissipation rate level of $\chi_{st} = 5000 \; 1/s$, representative of the characteristic aerodynamic straining intensity resolved in a uRANS fashion within the investigated pintle injector configuration. As shown in Fig. 6(a), the JL-9 mechanism tends to predict temperature peak values on the oxidizer-rich side of the flamelets, i.e., below the stoichiometric value $Z_{st} = 0.2$, which are also higher than the maximum

values returned by the Zhukov's mechanism. On the contrary, both the TSR-CDF-13 and the TSR-GP-24 kinetic schemes, analyzed in Figs. 6(b) and 6(c), respectively, provide consistent results with Zhukov's flamelet computations.

Similar considerations can be drawn from Fig. 7, which displays the mean temperature and root mean square (rms) temperature conditioned on Z. Again, the flame structure delivered by the JL-9 scheme is shifted toward mixture fraction values lower than the stoichiometric
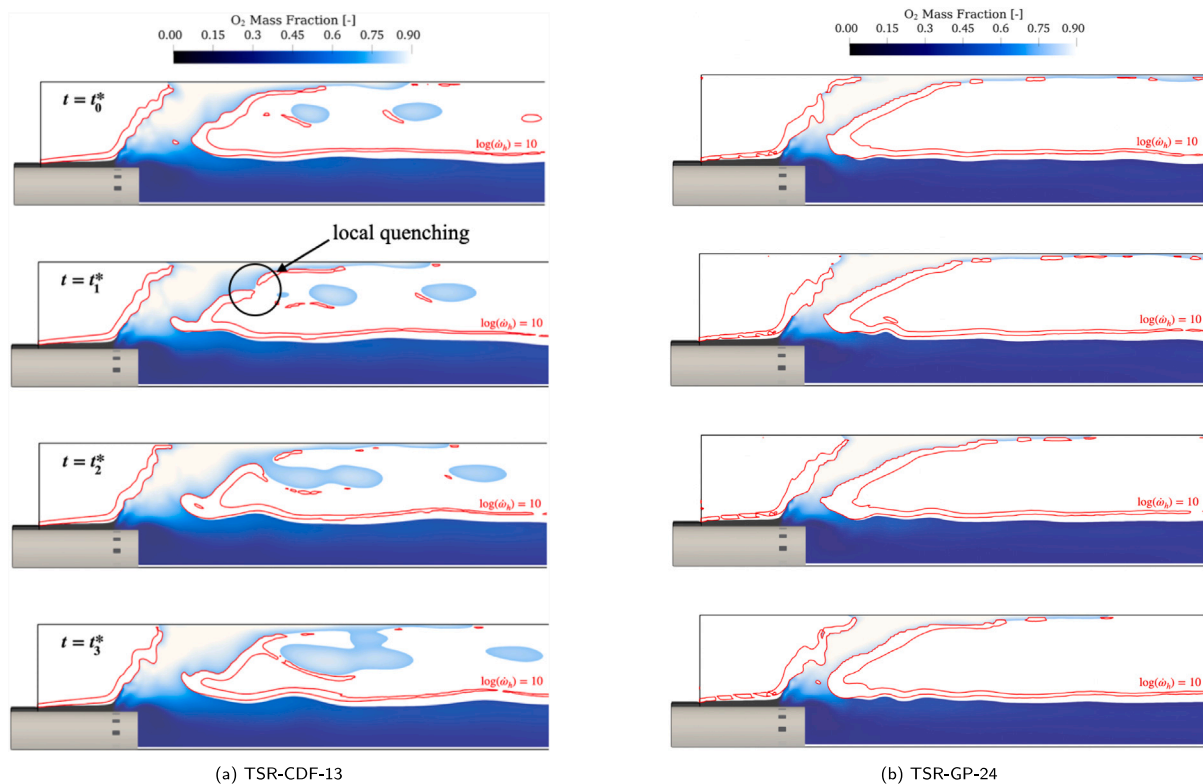
Fig. 8. From top to bottom, gaseous oxygen mass fraction contour map over a series of time instants, as predicted by: (a) TSR-CDF-13, (b) TSR-GP-24. Iso-lines of $\log(\dot{\omega}_h) = 10$ are shown in red. (For interpretation of the references to color in this figure legend, the reader is referred to the web version of this article.)

level, while the TSR-based skeletal mechanisms present practically identical flame structures.

To visualize the previously mentioned quenching phenomenon observed in the TSR-CDF-13 scheme, four consecutive time instants are analyzed in Fig. 8 concerning both the TSR-based skeletal mechanisms. Specifically, the oxygen mass fraction field is visualized in those regions where the formation of the main combustion products is not prominent yet, i.e., $Y_{CO} + Y_{CO_2} + Y_{H_2} + Y_{H_2O} \leq 0.25$, along with a single iso-level of the logarithmic heat release rate. As can be deduced from Fig. 8(a), the TSR-CDF-13 kinetic scheme features a quenching phenomenon localized on the final portion of the leeward shear layer, which triggers a release of oxygen pockets that can lead to additional reaction processes in the downstream region of the chamber, see also Fig. 3(b). On the contrary, the TSR-GP-24 mechanism does not exhibit any flame extinction, thus, the presence of gaseous oxygen is restrained upstream of the leeward front.

Further insights into the impact of chemical kinetic modeling on the predicted flame structure can be gained concerning the chemistry-turbulence interaction, which is characterized by the EDC mixing factor, k_{EDC} [59]. The temperature points in Fig. 6 are color-coded with k_{EDC}, highlighting that the JL-9 mechanism gives rise to a less significant turbulence damping effect compared with the TSR-CDF-13 and the TSR-GP-24 schemes. Indeed, most of the instantaneous temperature values in the proximity of the oxidizer-rich region exhibit k_{EDC} values close to 0.4, while the other two mechanisms feature lower values of the EDC mixing factor, resulting in more intense combustion-turbulence interaction. These aspects are corroborated by the contour maps of the instantaneous EDC mixing factor for the three simulations shown on the left panels in Fig. 10. Specifically, the highest values of k_{EDC}, denoting restrained damping effects induced by turbulence on the combustion process, can be envisaged within the final portions of the leeward and windward shear layer regions, regardless of the chemical mechanism under consideration. This spatial distribution results from the flow field induced by the jet-in-crossflow pintle configuration, as highlighted by

the mean radial velocity field reported on the right panels of Fig. 10. In fact, the interaction of the methane annular flow with the LOx radial jet induces the highest strain levels in correspondence with the impingement location, whereas turbulence intensity decays along the evolution of the shear layers. Nevertheless, the tendency of the JL-9 kinetic scheme to promote high-temperature values in oxidizer-rich regions results in maximum heat release rate levels within the final portion of the shear layer zone, see Fig. 3(a) and the iso-levels of Z in Fig. 10. Thus, the overall turbulence damping effect on the flame predicted by the JL-9 scheme results lower than those experienced by the remaining kinetic schemes.

Concerning the gas–liquid interaction and LOx spray evolution, Fig. 9 illustrates a three-dimensional visualization of computational parcels, scaled by their diameter and color-coded with the corresponding vaporization rate, i.e., $\dot{m}_{p,k}$ for the kth parcel in Eq. (8), along with mixture fraction and logarithmic heat release rate iso-levels. As stated above, the JL-9 quasi-global mechanism induces a peculiar flame pattern, completely surrounding the radial LOx jet. Consequently, meaningful differences in the spray vaporization process can be envisaged among the three numerical simulations. Indeed, the flame topology characterizing the JL-9 case promotes faster evaporation of the computational parcels. On the other hand, distinct windward and leeward flame fronts taking place under both TSR-CDF-13 and TSR-GP-24 kinetic modeling make this effect less evident. Furthermore, Fig. 9(b) highlights a peculiar behavior for the TSR-CDF-13 mechanism, which is not replicated by the TSR-GP-24 scheme. Notably, the iso-levels of the mean logarithmic heat release rate exhibit a non-continuous behavior on the leeward side of the flame, as a result of the aforementioned shedding phenomenon, investigated in Fig. 8.

To further characterize the latter, and to identify the underlying physical phenomenon triggering the quenching process, we conduct a TSR analysis on both the TSR-CDF-13 and the TSR-GP-24 kinetic schemes. Although a rigorous definition of the TSR can be found in [55,60], for the current purpose, it is worthwhile to recall that
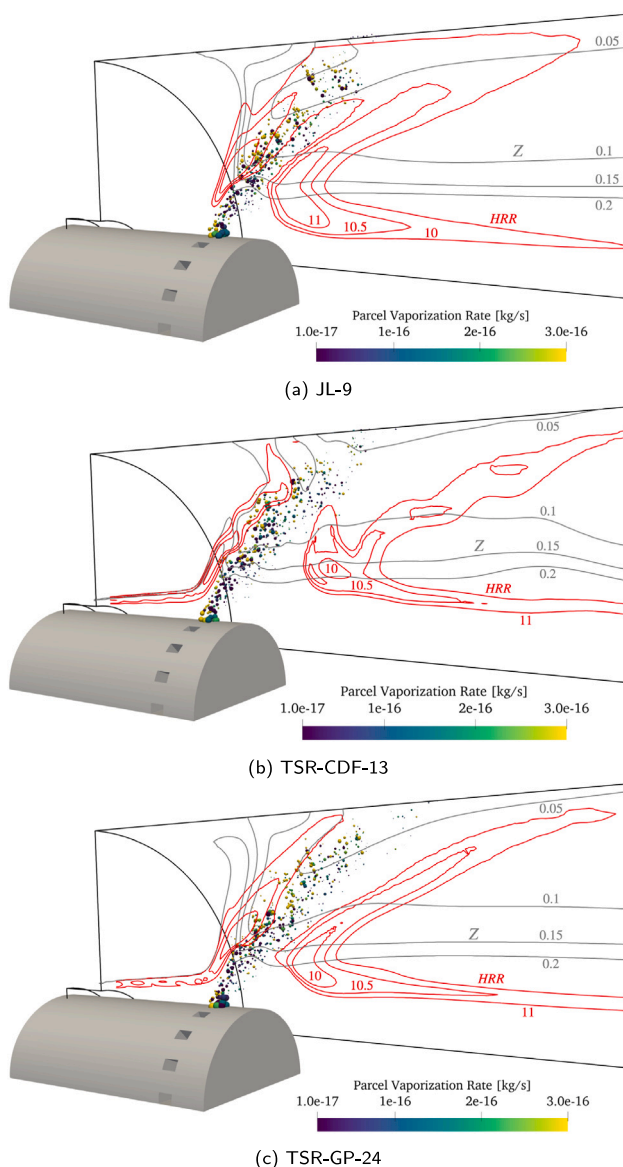
(a) JL-9

(b) TSR-CDF-13

(c) TSR-GP-24

Fig. 9. Three-dimensional visualization of the LOx jet, with computational parcels colored by their vaporization rate, as from Eq. (8), and scaled by their diameter. Iso-lines of the mean logarithmic heat release rate and mixture fraction are shown in red and gray, respectively. (For interpretation of the references to color in this figure legend, the reader is referred to the web version of this article.)

the inverse of the latter, hereinafter denoted as τ_{chem}, represents an integral scale of the chemical system under consideration in that it provides a direct measure of the most energy-containing time scale of the system. In this regard, Fig. 11 illustrates the contour map of the TSR-related chemical time scales – where $Y_{CO} + Y_{CO_2} + Y_{H_2} + Y_{H_2O} \leq 0.25$ and $\tau_{chem} \geq 1.0 \times 10^{-12}$ s – characterizing the Zhukov's skeletal mechanisms over four consecutive time instants, along with the logarithmic heat release rate iso-levels color-coded with k_{EDC}. In both instances, the highest characteristic chemical time scales are located in the proximity of the leeward shear layer, i.e., within oxidizer-rich regions. Still, the TSR-CDF-13 mechanism features higher values of the TSR-related time scales, namely, tending to $\tau = 1.0 \times 10^{-8}$ s, with increasing O/F values compared with the TSR-GP-24 scheme, as a consequence of the reduction strategy by which they were derived [39]. Nonetheless, due to the multi-physics nature of the problem under investigation, the chemistry-turbulence interaction further plays a key role in that the oxidizer-rich regions experiencing the slowest chemical

kinetic behavior also exhibit decreasing values of k_{EDC}. Therefore, in combination with the higher values of τ_{chem} characterizing the TSR-CDF-13 mechanism, this interaction eventually triggers the quenching phenomenon being observed.

Lastly, as one of the main outcomes of the present research study, we compare the combustion efficiency, η_{c*}, delivered by the three chemical mechanisms, and we discuss the overall computational cost, see Fig. 12. This way, we aim at providing an overview of a potential trade-off between the predictive accuracy and the cost affordability of variable-fidelity kinetic schemes targeting, from a practical engineering standpoint, the extensive use of large-scale design-oriented CFD. In this regard, significant discrepancies in the values of η_{c*} returned by the three mechanisms are evident from Fig. 12, and a monotonic trend with increasing mechanism complexity is envisaged. Moreover, the quasi-global JL-9 and the skeletal TSR-CDF-13 schemes exhibit 2.8% and 15% of the CPU cost characterizing the TSR-GP-24 mechanism, respectively. Notably, this non-linear behavior of the overall CPU cost results from increasing stiffness characterizing the ODE system embedded within the 13- and 24-species skeletal kinetic mechanisms [42]. Therefore, given the restrained increase in the computational burden from the JL-9 to the TSR-CDF-13 scheme, the latter should be always preferred over the quasi-global counterpart due to the extremely beneficial effects on the prediction of the flame pattern, see Fig. 6. Nonetheless, as shown in Fig. 8 concerning the local quenching phenomenon predicted by the TSR-CDF-13, the TSR-GP-24 mechanism still shows superior predictive performance. However, the complexity level introduced by the TSR-GP-24 is accompanied by unaffordable computational cost in view of design-oriented numerical campaigns conducted on LRE thrust chambers. Thus, to provide the community with cost-affordable, still reliable chemical mechanisms targeting methane–oxygen combustion under LRE-relevant thermodynamic conditions, we conclude that an optimal complexity level in skeletal mechanisms – possibly featured with optimization techniques [61] – should be pursued, while quasi-global kinetics should be regarded as an unreliable option.

4. Conclusions

In the present work, we investigated the impact of chemical modeling on the combustion characteristics of a LOx/GCH4 pintle injector configuration under rocket engine-relevant conditions. We carried out an extensive numerical analysis employing a hybrid Eulerian–Lagrangian unsteady Reynolds-averaged Navier–Stokes framework, by resorting to three different chemical kinetic mechanisms: (i) the 9-species quasi-global Jones-Lindstedt scheme, denoted as JL-9; (ii) a 13-species skeletal scheme derived from the high-pressure Zhukov's detailed mechanism, denoted as TSR-CDF-13; (iii) a 24-species skeletal scheme, derived from the same parent kinetic mechanism, and denoted as TSR-GP-24. Focusing on the major combustion observables, the thermal flow field, and the gas–liquid interaction, the numerical analysis revealed the following:

- The flow configuration that characterizes pintle injectors displays sensitivity to the type of mechanism employed. In particular, the quasi-global JL-9 mechanism predicts an unphysical flame structure, characterized by peak temperature values occurring in oxidizer-rich local mixtures. As a result, we observed a single flame front completely surrounding the cold oxygen core, which in turn affected the spray evolution and gas–liquid interaction. In contrast, both skeletal kinetic schemes predicted the presence of two distinct flame fronts, facilitating the extension of the liquid oxygen jet toward the upper chamber wall.
- Having demonstrated that a quasi-global mechanism may not be sufficient for accurately assessing these types of geometries, we observed that the choice of skeletal mechanism also significantly impacts the results. Notably, the use of the TSR-CDF-13 mechanism led to the emergence of a distinct oxygen shedding
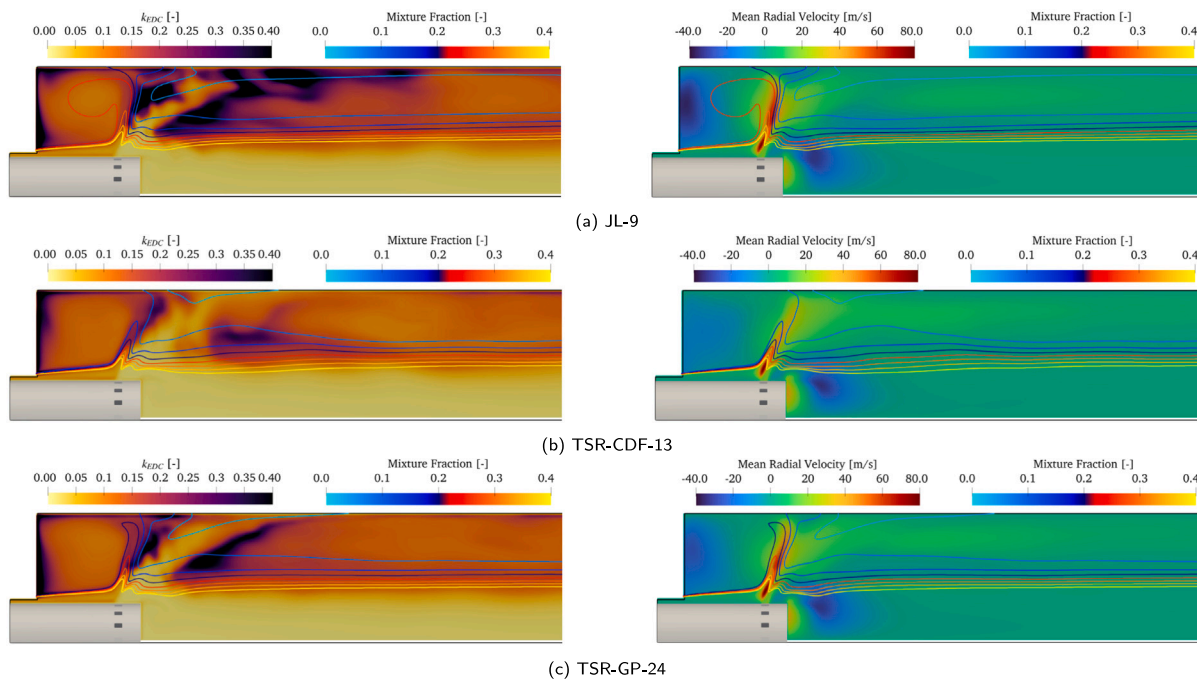
Fig. 10. Contour maps of the instantaneous EDC mixing factor, k_{EDC} (left), and mean radial velocity (right), as predicted by: (a) JL-9 scheme, (b) TSR-CDF-13 scheme, (c) TSR-GP-24 scheme. Solid lines represent iso-levels of the mean mixture fraction.
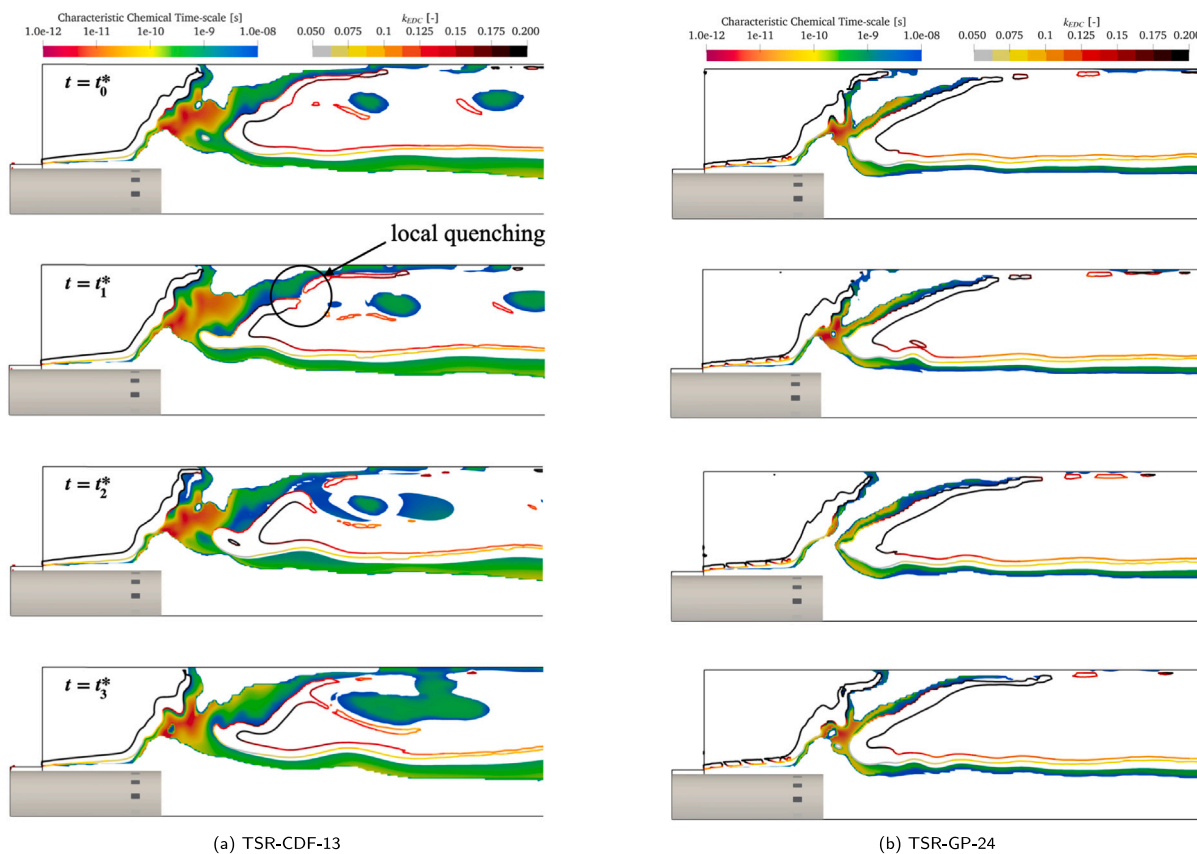

Fig. 11. From top to bottom, contour map of the characteristic chemical time scale returned by the TSR analysis over a series of time instants, as predicted by: (a) TSR-CDF-13, (b) TSR-GP-24. Iso-lines of $\log(\dot{\omega}_h) = 10$ are color-coded with the EDC mixing factor, k_{EDC}. (For interpretation of the references to color in this figure legend, the reader is referred to the web version of this article.)
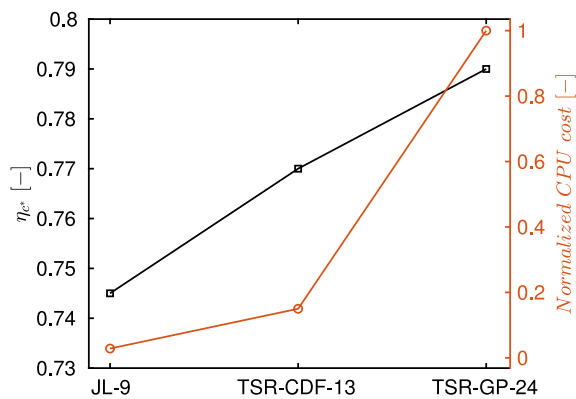
Fig. 12. Combustion efficiency, η_{c^*}, predicted by the three kinetic mechanisms (black line), and CPU cost normalized by $CPU_{TSR-GP-24}$ (red line). (For interpretation of the references to color in this figure legend, the reader is referred to the web version of this article.)

phenomenon, driven by a local quenching process on the leeward flame front. This phenomenon was initiated by a complex interplay of factors, including the notably large time scales inherent to the TSR-CDF-13 scheme in oxidizer-rich regions, turbulence-induced strain levels, and the spray evolution process.

- To ensure that results obtained from simulations are reliable and can be effectively used in the design of such devices, it is crucial to carefully select a kinetic mechanism tailored to capture all relevant combustion observables such as flame topology, thermal flow field, gas–liquid phase interaction, etc. This necessity is underscored by the notable discrepancies observed in terms of combustion efficiency among the three kinetic schemes.
- While quasi-global chemical kinetics do not yield reliable combustion predictions, an optimal balance between complexity and computational burden should be pursued when addressing the numerical characterization of liquid rocket engines through skeletal kinetic schemes, possibly featuring customized optimization strategies. In this context, TSR analysis has demonstrated its efficacy as a dependable diagnostic tool, offering valuable guidance in the selection and optimization of such mechanisms.

Declaration of competing interest

The authors declare that they have no known competing financial interests or personal relationships that could have appeared to influence the work reported in this paper.

Acknowledgments

References

[1] R. Roback, E.J. Szetela, L.J. Spadaccini, Deposit Formation in Hydrocarbon Rocket Fuels, NASA Contractor Report 165405, NASA Lewis Research Center, Cleveland, OH, 1981.

[2] T. Neill, D. Judd, E. Veith, D. Rousar, Practical uses of liquid methane in rocket engine applications, Acta Astronaut. 65 (5–6) (2009) 696–705.

[3] S.O. Starr, A.C. Muscatello, Mars in situ resource utilization: a review, Planet. Space Sci. 182 (2020) 104824.

[4] Matthew J. Casiano, James R. Hulka, Vigor Yang, Liquid-propellant rocket engine throttling: A comprehensive review, J. Propuls. Power 26 (5) (2010) 897–923.

[5] Gordon Dressler, J. Bauer, TRW pintle engine heritage and performance characteristics, in: 36th AIAA/ASME/SAE/ASEE Joint Propulsion Conference and Exhibit, Paper No. AIAA 2000-3871, 2000.

[6] Z. Sun, Y. Jia, H. Zhang, Technological advancements and promotion roles of Chang'e-3 lunar probe mission, Sci. China Technol. Sci. 56 (2013) 2702–2708.

[7] Fan Zhao, Hao Zhang, Haibin Zhang, Bofeng Bai, Liang Zhao, Review of atomization and mixing characteristics of pintle injectors, Acta Astronaut. 200 (2022) 400–419.

[8] Peng Cheng, Qinglian Li, Shun Xu, Zhongtao Kang, On the prediction of spray angle of liquid-liquid pintle injectors, Acta Astronaut. 138 (2017) 145–151.

[9] Huiyuan Chen, Qinglian Li, Peng Cheng, Experimental research on the spray characteristics of pintle injector, Acta Astronaut. 162 (2019) 424–435.

[10] R. Zhou, C. Shen, Experimental study on the spray characteristics of a pintle injector element, Acta Astronaut. 194 (2022) 255–262.

[11] M. Son, K. Yu, J. Koo, O.C. Kwon, J.S. Kim, Effects of momentum ratio and Weber number on spray half angles of liquid controlled pintle injector, J. Therm. Sci. 24 (2015) 37–43.

[12] Peng Cheng, Qinglian Li, Huiyuan Chen, Flow characteristics of a pintle injector element, Acta Astronaut. 154 (2019) 61–66.

[13] Wenyuan Zhou, Xu Xu, Qingchun Yang, Ronghui Zhao, Yushu Jin, Experimental and numerical investigations on the spray characteristics of liquid-gas pintle injector, Aerosp. Sci. Technol. (2022) 107354.

[14] Suji Lee, Daehwan Kim, Jaye Koo, Youngbin Yoon, Spray characteristics of a pintle injector based on annular orifice area, Acta Astronaut. 167 (2020) 201–211.

[15] Suji Lee, Jaye Koo, Youngbin Yoon, Effects of skip distance on the spray characteristics of a pintle injector, Acta Astronaut. 178 (2021) 471–480.

[16] Brunno B. Vasques, Oskar J. Haidn, Effect of pintle injector element geometry on combustion in a liquid oxygen/liquid methane rocket engine, in: 7th European Conference for Aeronautics and Aerospace Sciences, EUCASS, 2017.

[17] M. Son, K. Lee, J. Koo, Characteristics of anchoring locations and angles for GOX/GCH4 flames of an annular pintle injector, Acta Astronaut. 177 (2020) 707–713.

[18] Donghyuk Kang, Sanghoon Han, Chulsung Ryu, Youngsung Ko, Design of pintle injector using Kerosene-LOx as propellant and solving the problem of pintle tip thermal damage in hot firing test, Acta Astronaut. 201 (2022) 48–58.

[19] K. Radhakrishnan, M. Son, K. Lee, J. Koo, Effect of injection conditions on mixing performance of pintle injector for liquid rocket engines, Acta Astronaut. 150 (2018) 105–116.

[20] Min Son, Kanmaniraja Radhakrishnan, Youngbin Yoon, Jaye Koo, Numerical study on the combustion characteristics of a fuel-centered pintle injector for methane rocket engines, Acta Astronaut. 135 (2017) 139–149.

[21] Alessio Frassoldati, Alberto Cuoci, Tiziano Faravelli, ELISEO Ranzi, C Candusso, D Tolazzi, et al., Simplified kinetic schemes for oxy-fuel combustion, in: 1st International Conference on Sustainable Fossil Fuels for Future Energy, 2009, pp. 6–10.

[22] B.F. Magnussen, The eddy dissipation concept: A bridge between science and technology, in: ECCOMAS Thematic Conference on Computational Combustion, Lisbon, Portugal, 21-24 June 2005, 2005.

[23] Xin-xin Fang, Chi-bing Shen, Study on atomization and combustion characteristics of LOX/methane pintle injectors, Acta Astronaut. 136 (2017) 369–379.

[24] Jacopo Liberatori, Riccardo Malpica Galassi, Daniele Liuzzi, Antonio Filosa, Mauro Valorani, Pietro Paolo Ciottoli, Injection of LOX spray in Methane cross-flow RANS modeling uncertainty quantification, in: AIAA Propulsion and Energy Forum, Virtual Event, Paper No. AIAA 2021-3570, 2021.

[25] Patrick Jenny, Dirk Roekaerts, Nijso Beishuizen, Modeling of turbulent dilute spray combustion, Prog. Energy Combust. Sci. 38 (6) (2012) 846–887.

[26] Said Elghobashi, On predicting particle-laden turbulent flows, Appl. Sci. Res. 52 (1994) 309–329.

[27] S. Balachandar, John K. Eaton, Turbulent dispersed multiphase flow, Annu. Rev. Fluid Mech. 42 (2010) 111–133.

[28] X.-Q. Chen, JCF Pereira, Computation of turbulent evaporating sprays with well-specified measurements: a sensitivity study on droplet properties, Int. J. Heat Mass Transfer 39 (3) (1996) 441–454.

[29] Z. Naumann, L. Schiller, A drag coefficient correlation, Zeitschrift des Vereins Deutscher Ingenieure 77 (1935) 318–323.

[30] H.G. Weller, G. Tabor, H. Jasak, C. Fureby, A tensorial approach to computational continuum mechanics using object-oriented techniques, Comput. Phys. 12 (6) (1998) 620–631.

[31] D. Cavalieri, J. Liberatori, R. Malpica Galassi, P.E. Lapenna, M. Valorani, P.P. Ciottoli, Unsteady RANS simulations with uncertainty quantification of spray combustor under liquid rocket engine relevant conditions, in: AIAA SciTech 2023 Forum, National Harbor, MD & Online, Paper No. AIAA 2023-2148, 2023.

[32] Rolf D. Reitz, Rm Diwakar, Structure of High-Pressure Fuel Sprays, SAE Technical Paper 870598, 1987, pp. 1–18.

[33] G.P. Smith, D.M. Golden, M. Frenklach, N.W. Moriarty, B. Eiteneer, M. Goldenberg, C.T. Bowman, R.K. Hanson, S. Song, W.C. Gardiner, V. Lissianski, Z. Qin, GRI-mech 3.0, 1999, http://combustion.berkeley.edu/gri-mech/.

[34] C.-W. Zhou, Y. Li, U. Burke, C. Banyon, K.P. Somers, S. Ding, S. Khan, J.W. Hargis, T. Sikes, O. Mathieu, E.L. Petersen, M. AlAbbad, A. Farooq, Y. Pan, Y. Zhang, Z. Huang, J. Lopez, Z. Loparo, S.S. Vasu, H.J. Curran, An experimental and chemical kinetic modeling study of 1,3-butadiene combustion: Ignition delay time and laminar flame speed measurements, Combust. Flame 197 (2018) 423–438.

[35] E. Ranzi, C. Cavallotti, A. Cuoci, A. Frassoldati, M. Pelucchi, T. Faravelli, New reaction classes in the kinetic modeling of low temperature oxidation of n-alkanes, Combust. Flame 162 (5) (2015) 1679–1691.

[36] H. Wang, X. You, A.V. Joshi, S.G. Davis, A. Laskin, F. Egolfopoulos, C.K. Law, USC mech version II. High-temperature combustion reaction model of H2/CO/C1-C4 Compounds, May 2007, http://ignis.usc.edu/Mechanisms/USC-Mech%20II/USC_Mech%20II.htm.

[37] E.L. Petersen, D.F. Davidson, R.K. Hanson, Kinetics modeling of shock-induced ignition in low-dilution CH_4/O_2 mixtures at high pressures and intermediate temperatures, Combust. Flame 117 (1–2) (1999) 272–290.

[38] V.P. Zhukov, Kinetic model of alkane oxidation at high pressure from methane to n-heptane, Combust. Theory Model. 13 (3) (2009) 427–442.

[39] J. Liberatori, R. Malpica Galassi, D. Bianchi, F. Nasuti, M. Valorani, P.P. Ciottoli, Family of skeletal reaction mechanisms for methane-oxygen combustion in rocket propulsion, J. Propuls. Power (2024).

[40] G. Gargiulo, P.P. Ciottoli, E. Martelli, R. Malpica Galassi, M. Valorani, Numerical analysis of laser-pulse transient ignition of oxygen/methane mixtures in rocket-like combustion chamber, Acta Astronaut. 159 (June 2019) 136–155.

[41] S. Blanchard, Q. Cazères, B. Cuenot, Chemical modeling for methane oxy-combustion in Liquid Rocket Engines, Acta Astronaut. 190 (2022) 98–111.

[42] T. Lu, C.K. Law, Toward accommodating realistic fuel chemistry in large-scale computations, Prog. Energy Combust. Sci. 35 (2) (2009) 192–215.

[43] C.K. Westbrook, F.L. Dryer, Simplified reaction mechanisms for the oxidation of hydrocarbon fuels in flames, Combust. Sci. Technol. 27 (1–2) (1981) 31–43.

[44] W.P. Jones, R.P. Lindstedt, Global reaction schemes for hydrocarbon combustion, Combust. Flame 73 (1988) 233–249.

[45] N. Peters, R.J. Kee, The computation of stretched laminar methane-air diffusion flames using a reduced four-step mechanism, Combust. Flame 68 (1) (1987) 17–29.

[46] S.H. Lam, D.A. Goussis, The CSP method for simplifying kinetics, Int. J. Chem. Kinet. 26 (1994) 461–486.

[47] T. Lu, C.K. Law, A directed relation graph method for mechanism reduction, Proc. Combust. Inst. 30 (1) (2005) 1333–1341.

[48] P. Pepiot-Desjardins, H. Pitsch, An efficient error-propagation-based reduction method for large chemical kinetic mechanisms, Combust. Flame 154 (1–2) (2008) 67–81.

[49] T. Nagy, T. Turányi, Reduction of very large reaction mechanisms using methods based on simulation error minimization, Combust. Flame 156 (2) (2009) 417–428.

[50] W. Sun, Z. Chen, X. Gou, Y. Ju, A path flux analysis method for the reduction of detailed chemical kinetic mechanisms, Combust. Flame 157 (7) (2010) 1298–1307.

[51] R. Malpica Galassi, M. Valorani, H.N. Najm, C. Safta, M. Khalil, P.P. Ciottoli, Chemical model reduction under uncertainty, Combust. Flame 179 (May 2017) 242–252.

[52] R. Malpica Galassi, P.P. Ciottoli, S.M. Sarathy, H.G. Im, S. Paolucci, M. Valorani, Automated chemical kinetic mechanism simplification with minimal user expertise, Combust. Flame 197 (1) (2018) 1125–1133.

[53] Riccardo Malpica Galassi, PyCSP: a Python package for the analysis and simplification of chemically reacting systems based on computational singular perturbation, Comput. Phys. Comm. 276 (2022) 108364, URL https://www.sciencedirect.com/science/article/pii/S0010465522000832.

[54] P.P. Ciottoli, R. Malpica Galassi, P.E. Lapenna, G. Leccese, D. Bianchi, F. Nasuti, F. Creta, M. Valorani, CSP-based chemical kinetics mechanisms simplification strategy for non-premixed combustion: An application to hybrid rocket propulsion, Combust. Flame 186 (2017) 83–93.

[55] M. Valorani, P.P. Ciottoli, R. Malpica Galassi, Tangential stretching rate (TSR) analysis of non premixed reactive flows, Proc. Combust. Inst. 36 (1) (2017) 1357–1367.

[56] Jonas Bredberg, On the Wall Boundary Condition for Turbulence Models, Internal Report 00/4. G oteborg, Chalmers University of Technology, Department of Thermo and Fluid Dynamics, 2000, pp. 8–16.

[57] D. Papamoschou, A. Roshko, The compressible turbulent shear layer : an experimental study, J. Fluid Mech. 197 (1988) 453–477.

[58] R.W. Bilger, S.H. Stårner, R.J. Kee, On reduced mechanisms for methane air combustion in nonpremixed flames, Combust. Flame 80 (2) (1990) 135–149.

[59] I.S. Ertesvåg, Analysis of some recently proposed modifications to the eddy dissipation concept (EDC), Combust. Sci. Technol. 192 (6) (2020) 1108–1136.

[60] M. Valorani, S. Paolucci, E. Martelli, T. Grenga, P.P. Ciottoli, Dynamical system analysis of ignition phenomena using the tangential stretching rate concept, Combust. Flame 162 (8) (2015) 2963–2990.

[61] Jacopo Liberatori, Riccardo Malpica Galassi, Mauro Valorani, Pietro Paolo Ciottoli, CSP-driven optimization of a 16-species skeletal mechanism for methane ignition at high pressure, in: AIAA SciTech 2023 Forum, National Harbor, MD & Online, Paper No. AIAA 2023-1101, 2023.